Chemical Engineering Journal 526 (2025) 171300

Contents lists available at ScienceDirect

Chemical Engineering Journal

journal homepage: www.elsevier.com/locate/cej

Covalency modulated by Fe-F-Fe configuration and oxygen vacancy promotes dual mechanism for oxygen evolution reaction

Bo Feng [a], Keyi Lv [a], Ziyong Zhang [a,b], Nianwen Song [a], Ziyang Yan [a], Yuchao Zhang [a], Yanfei Wei [a], Xiaofei Yu [a], Lanlan Li [a], Xinghua Zhang [a], Xiaojing Yang [a], Zunming Lu [a,*], Juntao Huo [b,*]

[a] School of Materials Science and Engineering, Hebei University of Technology, Tianjin, 300130, China
[b] CAS Key Laboratory of Magnetic Materials and Devices, Zhejiang Province Key Laboratory of Magnetic Materials and Application Technology, Ningbo Institute of Materials Technology and Engineering, Chinese Academy of Sciences, Ningbo, 315201, China

ARTICLE INFO

Keywords:
Adsorbate evolution mechanism
Single metal site mechanism
Covalency
Deprotonation
O-O coupling

ABSTRACT

Early transition metal oxide electrocatalysts are advanced materials for replacing noble metal catalysts for efficient electrocatalytic water splitting. Precise modulation of the local coordination environment in catalysts poses significant challenges in identifying interatomic synergistic effects on catalytic surfaces and deciphering the underlying reaction mechanisms. Here, we significantly enhance the covalency of Fe-O bond and the synergistic catalytic effect between surface metal and oxygen atoms by introducing fluorine anion and oxygen vacancy defects on the $NiFe_2O_4$ (3 1 1) surface. Experimental and theoretical calculations show that the prepared catalysts carry out the OER process through the adsorbate evolution mechanism (AEM) and the single-metal-site mechanism (SMSM). Oxygen vacancy and fluorine anion can increase d-d coulomb interactions, optimize lower Hubbard band (LHB) positions, and improve deprotonation of surface metal sites and O-O coupling of lattice oxygen sites while promoting AEM and SMSM. The Fe_{Oh}-F-Fe_{Td} configuration has the strongest intrinsic activity and the best intermediate adsorption energy. In alkaline media, the F60 catalyst has a low overpotential of 271 mV at a current density of 10 mA cm^{-2} and stability over 100 h at 100 mA cm^{-2}. This work provides insights into identifying the true active site and catalytic mechanism of the catalysts.

1. Introduction

Hydrogen energy is a key component in achieving the global energy transition, and electrocatalytic water splitting is the primary method for producing green hydrogen [1,2]. The four-electron process of the oxygen evolution reaction (OER) at the anode leads to high reaction energy barriers and slow reaction kinetics [3,4]. In revealing the catalytic pathways of OER, the researchers proposed the adsorbed evolution mechanism (AEM) [5], lattice oxygen mediated mechanism (LOM) [6], and O-O coupling mechanism (OPM) [7]. AEM utilizes a metal as the active site, which is limited by the linear energy relationship between the reaction intermediates, resulting in catalytic activity with a theoretical overpotential of 0.37 V [8]. LOM uses lattice oxygen as the redox center, effectively avoiding high energy barriers due to *O-OH coupling [9]. The proton and electron transfer processes in LOM are decoupled, unlike in AEM. LOM can also be subdivided into the oxygen-vacancy-site mechanism (OVSM) and the single-metal-site mechanism (SMSM) [10]. The difference between SMSM and OVSM is in the adsorption site of *OH. OVSM uses lattice oxygen as the adsorption site for *OH. SMSM adsorbs *OH at a metal site, subsequently undergoes a deprotonation step, and couples the adsorbed oxygen with lattice oxygen. However, LOM tends to undergo structural collapse and deactivation on the catalyst surface due to the involvement of lattice oxygen in the reaction, which can result in instability. The active sites of OPM are adjacent metal atoms, which enables both avoidance of *O-OH coupling and high structural stability. The activation of OPM is more difficult to realize as it requires a moderate distance between adjacent metal sites and an optimal adsorption strength for the reaction intermediates [11]. Identifying the real active sites and elucidating the authentic catalytic mechanisms of catalysts are essential for designing efficient catalysts.

The diversity of catalytic pathways provides abundant options for enhancing catalyst activity, but also presents challenges for identifying

* Corresponding authors.
E-mail addresses: luzunming@hebut.edu.cn (Z. Lu), huojuntao@nimte.ac.cn (J. Huo).

https://doi.org/10.1016/j.cej.2025.171300
Received 9 September 2025; Received in revised form 16 November 2025; Accepted 25 November 2025
Available online 26 November 2025

active sites and elucidating catalytic mechanisms [12]. Doping and vacancy engineering can effectively modulate reaction pathways [13,14]. However, the surface heterogeneity induced during such regulation, synergistic effects among surface atoms, and the unpredictability of dynamic evolution at the catalyst surface under reaction conditions pose fundamental challenges in elucidating active centers with atomic precision. Current researches predominantly focus on single catalytic mechanism, which fail to combine the advantages of both the AEM and LOM [15]. Therefore, the rational design of catalysts that integrate active metal sites and lattice oxygen sites with enhanced redox properties is critically important.

$NiFe_2O_4$ is a typical transition metal oxide with an anti-spinel oxide (AB_2O_4) structure [16]. Its structural unit consists of densely packed rows of oxygen anions, with Ni^{2+} and a portion of Fe^{3+} occupying the center of the oxygen octahedron (Oh), and the remaining Fe^{3+} occupying the oxygen tetrahedral (Td) coordination site [17]. Although $NiFe_2O_4$ demonstrates moderate activity in both the AEM and LOM, its overall catalytic performance remains constrained by intrinsically low activity and a limited density of surface active sites [18]. Recent research has developed modulation methods to optimize the electronic structure and increase the number of active sites to enhance catalytic activity, including ion doping [19], vacancy engineering [20], and morphology modulation [21]. Recent evidence suggests that oxygen vacancies serve as effective activators of lattice oxygen reactivity [22], and non-metallic ions doping tailors the electronic properties of metal sites [23,24]. Research indicates that both strategies effectively enhance the covalency of M-O bonds [25,26]. This optimization improves the catalytic activity of metal or lattice oxygen sites, potentially enabling mechanism switching or enhancing activity and stability. Combining these methods shows great potential for coupling metal and oxygen sites to design hybrid catalysts that utilize both AEM and LOM pathways.

In this work, we designed $NiFe_2O_4$ catalysts co-modified with fluorine anion (F) and oxygen vacancy (Ov), which can enhance the deprotonation ability of the metal sites and the coupling of lattice oxygen to adsorbed oxygen, resulting in coupling of AEM and SMSM. Experimental results show that modification with F and oxygen vacancy regulates the electronic structure of Fe and O sites, that leads to shortened Fe-O bond length and enhanced covalency of Fe-O. Therefore, the catalyst exhibits enhanced dual mechanism activity. Theoretical calculations reveal that Fe-F-Fe and oxygen vacancy adjust the positional relationship between the lower Hubbard band and the 2*p* orbital of oxygen, thereby enhancing the deprotonation and O-O coupling ability. We demonstrate that the Fe_{Oh}-F-Fe_{Td} configuration on the catalyst (3 1 1) plane exhibits an optimal reaction energy barrier and effectively activates the lattice oxygen of the Fe-O bond while facilitating the AEM and SMSM mechanisms to improve performance and stability. The design strategy and the analysis of active sites and catalytic mechanisms of this work have important implications for the design of catalysts.

2. Experimental details

2.1. Methods

2.1.1. Preparation of $NiFe_2O_4$

$NiFe_2O_4$ nanoparticles were prepared by solvothermal method. 0.5 mmol of $Ni(CH_3COO)_2{\cdot}4H_2O$ and 1 mmol of $Fe(NO_3)_3{\cdot}9H_2O$ were dissolved in 40 mL of deionized water and stirred for 1 h at room temperature. Dissolve 1.2 g NaOH in 10 mL deionized water and sonicate until uniformly dispersed. The NaOH solution was slowly added to the metal salt solution and stirred for 2 h until well mixed. The obtained suspension was transferred to a 100 mL polytetrafluoroethylene reactor and reacted for 15 h at 180 °C. After cooling naturally, the sample was washed several times by centrifugation using ethanol and deionized water, and dried at 60 °C. A sample of $NiFe_2O_4$ nanoparticles was obtained, named NFO.

2.1.2. Preparation of oxygen vacancy modified $NiFe_2O_4$

Dissolve 0.115 mg of $NaBH_4$ in 30 mL of deionized water. 50 mg of NFO was taken and added to the $NaBH_4$ solution and immersed for 30 min. Subsequent centrifugal washing using ethanol and deionized water several times and drying at 60 °C obtained oxygen vacancy-modified $NiFe_2O_4$, named OV.

2.1.3. Preparation of fluorine anion and oxygen vacancy co-modified $NiFe_2O_4$

Grind 30 mg OV with 30 mg NH_4F for 30 min and mix well. The precursor was heated up to 300 °C at 2 °C/min under N_2 atmosphere and held for 2 h to obtain the fluorine anion and oxygen vacancy modified catalyst, named F30. Using a similar method, the sample obtained using 60 mg NH_4F was named F60.

2.2. Physical characterizations

The crystal structure of the catalysts was characterized using an X-ray diffractometer (XRD, Bruker D8 Discover) under Cu Kα radiation. The micro-morphology of the catalysts was characterized using scanning electron microscopy (SEM, TESCAN MIRA LMS) and transmission electron microscopy (TEM, FEI Talos F200x). The catalyst surface chemical bonds were analyzed using a Raman spectrometer (Raman, LabRAM HR Evolution) using an excitation wavelength of 532 nm. The surface chemical states of the catalysts were analyzed using X-ray photoelectron spectroscopy (XPS, ESCALAB 250Xi). The oxygen vacancies were characterized using an electron paramagnetic resonance spectrometer (EPR, Bruker ESR5000). A Bruker INVENIO S spectrometer equipped with a liquid nitrogen-cooled mercury cadmium telluride (MCT) detector was used for in situ attenuated total reflection Fourier transform infrared (ATR-FTIR) analysis. The electronic and coordination structures of the catalysts were analyzed using a benchtop X-ray absorption fine structure spectrometer (easyXAFS300). The elemental composition of the catalysts was analyzed using an inductively coupled plasma mass spectrometer (ICP-MS, Thermo iCAP TQ). The content of isotopic oxygen atoms was analyzed using a differential electrochemical mass spectrometer (DEMS LingLu QAS100).

2.3. Electrochemical measurement

The OER performance of the catalysts under 1 M KOH electrolyte was tested on a Chenhua CHI 760E electrochemical workstation using a standard three-electrode system. An electrode of saturated calomel (SCE), a carbon rod and a glassy carbon electrode (GCE) were used as reference, counter and working electrodes, respectively. Catalyst ink was obtained by dispersing 5 mg of catalyst and 5 mg of carbon black in 480 μL of deionized water and 480 μL of isopropanol, adding 40 μL of Nafion solution, and sonicating for 1 h.

The test potential was converted to a reversible hydrogen electrode (RHE) potential by the Nernst equation: $E_{RHE} = E_{SCE} + 0.244 + 0.059*pH$. The catalyst was fully activated using a CV test with a sweep rate of 50 mV s^{-1} (test interval of 0–0.5 V vs. SCE). LSV tests were performed at 5 mV s^{-1} (test interval of 0–0.8 V vs. SCE) with 95 % IR compensation to correct the potential. Electrochemical impedance spectra (EIS) were tested in the frequency range of 0.1–100 kHz at 0.5 V vs. SCE. The double-layer capacitance (C_{dl}) was obtained by testing CV curves from 5 to 30 mV s^{-1} in the interval 0.1–0.15 V vs. SCE. The turnover frequency (TOF) of the catalyst was calculated to evaluate its intrinsic activity with the following equation: $TOF = (j*S)/(n*F*N)$. j is the current density, S is the electrode area, n is the number of electron transfers, F is the Faraday constant, and N is the number of active sites.

2.4. Calculation details

DFT calculations using the VASP package (Vienna Ab-inition Simulation Package) with projector-augmented wave (PAW)

pseudopotentials [27,28]. The exchange-correlation interactions between the valence electrons were taken into account using the Perdew-Burke-Ernzerhof (PBE) functional within the generalized gradient approximation (GGA). The Brillouin zone was sampled using a $3 \times 3 \times 1$ k-point grid, and the cutoff energy was set to 450 eV. The energy convergence accuracy was set to 10^{-5} eV, and the force convergence accuracy to 0.03 eV $Å^{-1}$. The strong electronic interactions were corrected using DFT + U with the equivalent U-J values of the Hubbard parameter set to 6.4 and 5.5 eV for Ni and Fe [29–31]. The crystal orbital Hamiltonian layout (COHP) of the atomic pairs was calculated using the Lobster program [32]. The LHB and UHB are determined by the 3d orbitals below and above the Fermi energy level of the DOS, respectively.

3. Results and discussion

3.1. Crystal structure and morphology

The synthesis process is shown in Fig. 1a. $NiFe_2O_4$ (named NFO) is synthesized via a hydrothermal method, $NiFe_2O_4$ with a certain oxygen vacancy concentration (named OV) is synthesized by reduction using $NaBH_4$, and catalysts modulated by fluorine anion and oxygen vacancy (named F30 and F60) are subsequently synthesized by milling and uniformly heat-treating with NH_4F. The results of X-ray diffraction patterns (XRD) show that the diffraction peaks of the synthesized catalysts are well matched with the standard cards (PDF#74–2081) and correspond to the (1 1 1) (2 2 0) (3 1 1) (2 2 2) (4 0 0) (4 2 2) (5 1 1) (4 4 0) crystal planes of $NiFe_2O_4$, which suggests that the synthesized catalysts have a typical anti-spinel structure (Fig. S1). XRD Rietveld refinement results show that all samples exhibit a face centered cubic structure

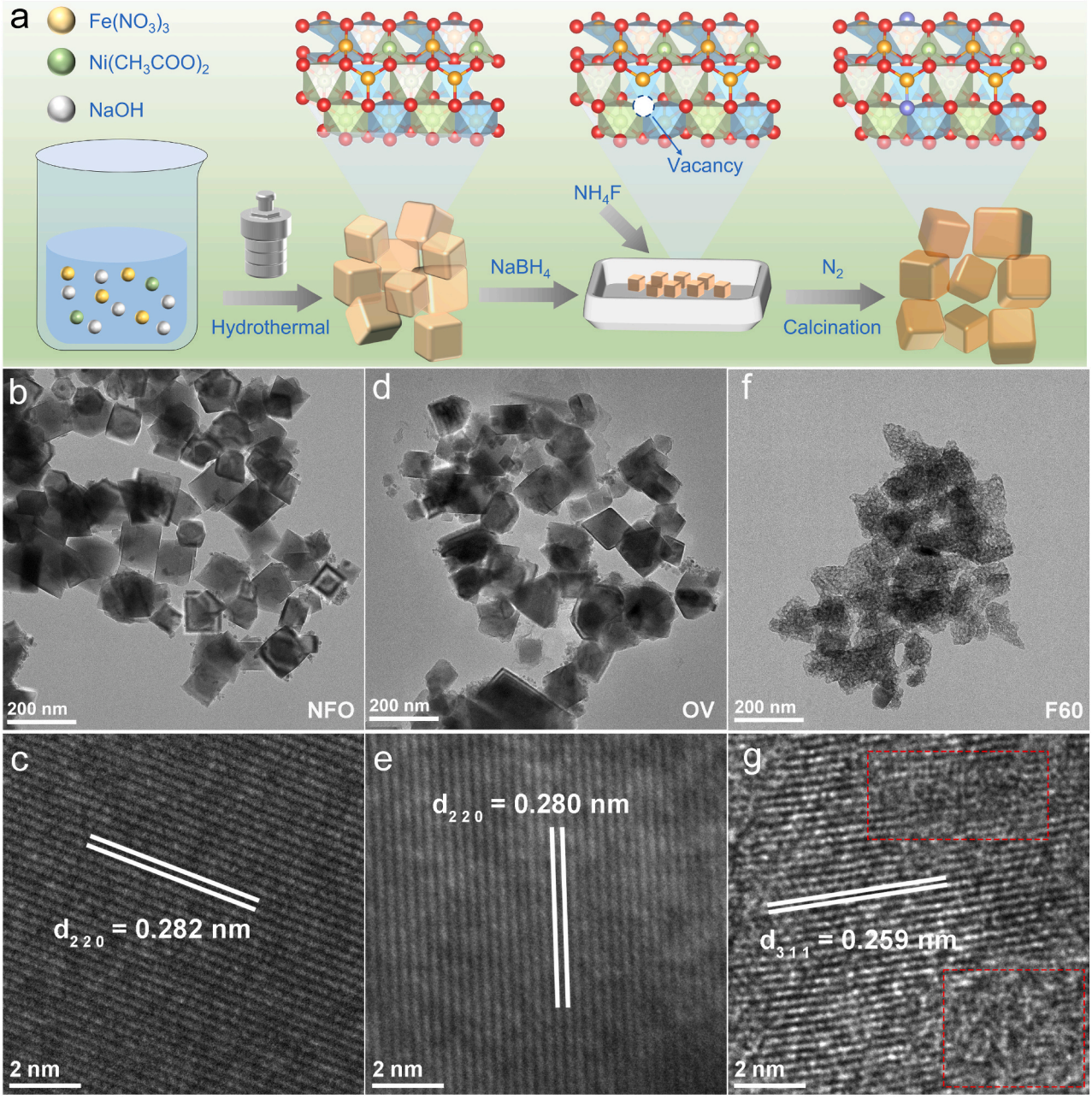

Fig. 1. Synthesis and morphology of the catalysts. a) Synthesis process of the catalysts. TEM and HRTEM images of b, c) NFO, d, e) OV and f, g) F60.

(space group Fd⁻3 m), with F30 (a = 8.3619 Å) and F60 (a = 8.3627 Å) exhibiting a significant increase in lattice parameter compared to NFO (a = 8.3536 Å) and OV (a = 8.3521 Å), indicating the presence of crystal cell expansion (Fig. S2). This suggests a possible change in bond lengths within the system due to cell expansion [33].

Fig. S3 shows the scanning electron microscopy (SEM) images of the catalysts; the morphology of NFO and OV is dominated by nanoparticles, and the SEM images of F30 and F60 show the presence of some irregular particles. In addition, energy dispersive spectroscopy (EDS) indicated that the elements of Ni, Fe, O, and F are uniformly distributed (Figs. S4 and S5), and the content of element F in F30 and F60 is 2.21 % and 5.99 %, respectively (Table S1). Fig. 1b-e illustrates the transmission electron microscopy (TEM) images and the high-resolution transmission electron microscopy images (HRTEM) of NFO and OV. The NFO nanoparticles exhibit a predominantly nano-cubic morphology with a highly regular shape, indicative of their high crystallinity. The exposed crystal plane of the NFO is (2 2 0), with a spacing of 0.282 nm. The morphology of the OV remains largely unchanged following $NaBH_4$ reduction, with the (2 2 0) crystal plane exhibiting an spacing of 0.280 nm.

Figs. 1f,g and S6,7 present the TEM and HRTEM images of F30 and F60, revealing that both samples exhibit two distinct morphological characteristics. A portion of the catalysts retains the nanoparticle morphology, with the exposed crystal plane corresponding to the (2 2 0) crystal plane. The other portion results from the etching effect of HF generated by the pyrolysis of NH_4F. This etching transforms the cubic structures into irregular particles with rough surfaces. The exposed crystal plane is predominantly the (3 1 1) plane, with lattice spacings of 0.258 nm and 0.259 nm corresponding to F30 and F60, respectively. The region inside the red line in Fig. 1g exhibits obvious lattice distortions, revealing a high density of surface defects after HF etching, which may have a significant impact on the electronic structure of the catalyst. The (3 1 1) crystal plane with a high density of defects may exhibit distinct catalytic properties compared to the (2 2 0) plane. The elemental mapping of TEM shows that Ni, Fe, O and F are uniformly distributed in the corresponding catalysts (Figs. S8 and S9). The ICP results confirm that the ratio of Ni and Fe elements in all catalysts is around 1:2, which is

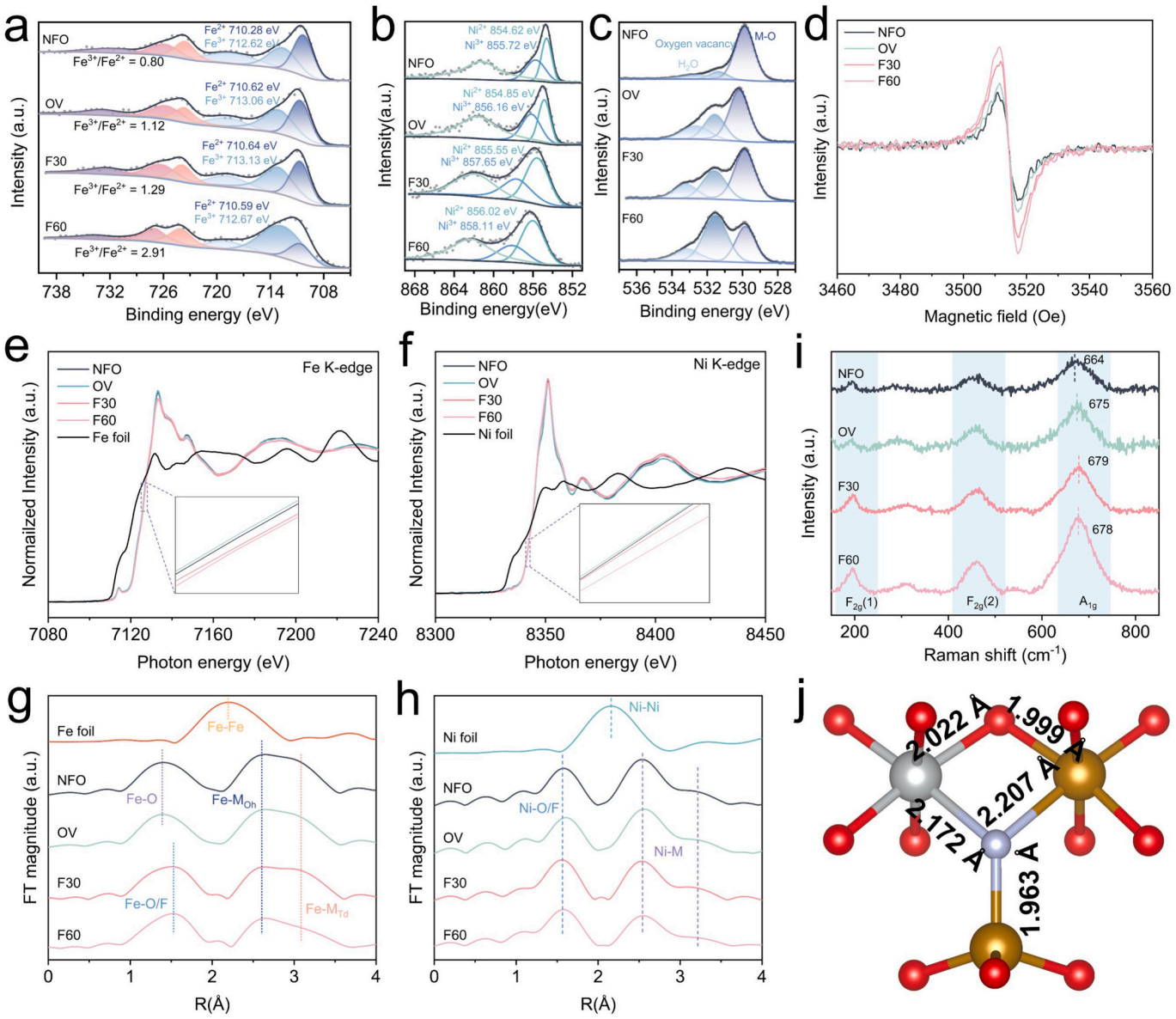

Fig. 2. Elemental valence and coordination structures of catalysts. High-resolution XPS spectra of a) Fe 2*p*, b) Ni 2*p*, c) O 1 *s*. d) EPR spectra of the samples. e) Fe K edge XANES spectra of the samples. f) Ni K edge XANES spectra of the samples. g) Fe and h) Ni FT-EXAFS spectrum. i) Raman spectrum of the catalyst. j) Effect of F replacement of the central oxygen atom on the bond length.

consistent with the EDS results (Table S2).

3.2. Electronic structure and coordination environment

The peak located near 684 eV in the XPS spectrum of F 1*s* represents the M-F bond in catalysts, indicating the successful doping of F ions (Figs. S10 and S11) [34]. Fig. 2a demonstrates the high-resolution Fe 2*p* XPS spectra, with the main Fe $2p_{3/2}$ peak of NFO splitting into two peaks of Fe^{2+} (710.28 eV) and Fe^{3+} (712.62 eV) [35]. Both peak positions of Fe $2p_{3/2}$ of the other catalysts are shifted to higher binding energy compared to the pristine NFO with a significantly increased Fe^{3+}/Fe^{2+} ratio. These results indicate an increase in the average valence state of Fe on catalyst surface. Fig. 2b demonstrates the high-resolution Ni $2p_{3/2}$ XPS spectra, with the main Ni $2p_{3/2}$ peak of NFO splitting into two peaks of Ni^{2+} (854.62 eV) and Ni^{3+} (855.72 eV) [36]. The average valence state of surface Ni is also increased, as indicated by the shift to higher binding energy. Elevated valence states of Fe and Ni can facilitate the formation of electron-ligand holes on oxygen ligands, contributing to the enhancement of lattice oxygen activity [37]. The high-resolution XPS spectrum of O 1*s* splits into three peaks representing M-O bonds, oxygen vacancies, and adsorbed water molecules. Moreover, the proportion of peaks corresponding to oxygen vacancies progressively increases, indicating a rising concentration of oxygen vacancy (Fig. 2c and Table S3) [38]. The variation in oxygen vacancy concentration of the catalysts is further confirmed by EPR, with the relative concentration following the order F60 > F30 > OV > NFO (g = 2.003). This result verifies that the increase in oxygen vacancy concentration in OV is attributed to $NaBH_4$ reduction, while the even higher concentrations observed in F30 and F60 are a consequence of HF etching (Fig. 2d). A high oxygen vacancy concentration can also promote the structural optimization of M-O bonds and enhance their intrinsic catalytic activity [39].

The localized atomic and electronic structures of the catalysts are investigated using X-ray absorption near edge structure (XANES) and extended X-ray absorption fine structure (EXAFS). Fig. 2e presents the Fe K edge XANES spectra, demonstrating that the Fe valence states in the samples decrease in the order of F60, F30, NFO, and OV. The Ni K edge XANES spectra shows the same pattern of valence change (Fig. 2f). The trend in the valence state changes of OV is opposite to that of the XPS results. All the elemental binding energy on the OV surface are shifted to higher binding energy. We attribute this phenomenon to the increase in the content of surface oxygen vacancy and the increase in the number of free electrons on the surface, which can accelerate the directional transfer of electrons from the catalyst surface to the bulk phase (Fig. S12) [40]. Meanwhile, oxygen vacancy accumulate on the catalyst surface after NFO undergoes reduction with $NaBH_4$, while their concentration in the bulk phase remains lower. High concentrations of oxygen vacancy at the surface cause structural distortion in the surface layer, altering the M-O coordination structure and thereby affecting the localized charge distribution (Fig. S13). The white line peak intensity of the Fe K edge of F30 and F60 is significantly lower compared with that of NFO and OV (Fig. 2e), and the white line peak intensity of the K edge of Ni is basically unchanged (Fig. 2f). In general, the white line peak is associated with the transition of the electron from the 1*s* orbital to the 4*p* orbital. For the M-O ligand, the intensity of the white line peak can reflect the degree of deformation of the ligand [41]. This indicates a larger degree of distortion of the Fe-O ligand and a lesser degree of deformation of the Ni-O ligand for F30 and F60.

The localized coordination environment is further investigated using Fourier transform extended X-ray absorption fine structure (FT-EXAFS) (Figs. 2g,h and S14–16). The first shell layer peak located at 1.5 Å in Fig. 2g corresponds to the Fe-O/F bond [10], which exhibits a significant increase in bond lengths for F30 and F60 compared to NFO and OV. This increase can be attributed to the elongation of Fe-F bonds caused by F doping, with the Fe-F bond length (F60, 1.942 Å) being longer than that of the Fe-O bond length (F60, 1.862 Å). The fitting results show that the Fe-O bond lengths become progressively shorter with the introduction of oxygen vacancy and F doping, with a specific trend of NFO (1.942 Å) > OV (1.941 Å) > F30 (1.878 Å) > F60 (1.862 Å) (Table S4). The reduction in bond length signifies an enhancement in covalency. For metal-active centers, strong M-O covalency facilitates rapid charge transfer between surface metal cations, ligand oxygen and reaction intermediates [42]. And it also can active lattice oxygen thus accelerating OER. The two second shell layer peaks present around 2.6 Å and 3.1 Å are attributed to the Fe-M_{oh} and Fe-M_{Td} bonds [30], and the reduced peak intensities indicate the increased degree of structural distortion. The Ni-O bond length of OV (2.049 Å) is slightly increased relative to the pristine NFO (2.047 Å), whereas the Ni-O bond lengths of F30 and F60 are reduced to 2.041 Å and 2.029 Å, respectively. Moreover, the decrease in the peak strength of the Ni-M bond is consistent with that of the Fe-M bond, suggesting a deformation of the coordination structure (Fig. 2h and Table S5) [43]. The FT-EXAFS spectra of Ni do not exhibit a significant shift in the Ni-F bond length, indicating that F preferentially coordinates with Fe atoms. This conclusion is further supported by the coordination number analysis, which reveals that the coordination number of Fe-F (F60, CN = 1.1) is higher than that of Ni-F (F60, CN = 0.5). The overall coordination number of M-O/F exhibits a decreasing trend, indicating an increase in oxygen vacancy concentration. This conclusion is consistent with the EPR results. Wavelet transform (WT-EXAFS) analysis shows the presence of M-O and M-O-M bonds in the samples, which are identical to the FT-EXAFS results (Fig. S17).

Fig. 2i presents the Raman spectrum (Raman) of catalysts, with the peak at 670 cm^{-1} (A_{1g}) corresponding to the lattice vibration at the octahedral position [44]. The blue shift of the A_{1g} peak indicates a decrease in the M-O bond length at the octahedral site of the catalysts [31]. There is a tendency for the A_{1g} peak pattern to broaden toward lower frequencies due to the larger length of the M-F bond, indicating the emergence of the M-F bond. The F_{2g} vibrational modes are associated with asymmetric stretching and bending at tetrahedral and octahedral positions [16]. The increased intensities of the F_{2g} peak in F30 and F60 confirm a higher degree of structural distortion. Based on the above investigations, F atoms tend to be coordinated with two Fe atoms and one Ni atom (Fig. 2j). Combined with the optimized results of theoretical calculations, the M-F bond is longer than the M-O bond, and the M-O bond length of the remaining coordination decreases, which can increase the covalency of the M-O bond and increase its catalytic activity. It is remarkable that the Fe-O bond length is significantly shorter than that of Ni-O. And the Fe-O bond is more disturbed under the modifications of fluorine anion and oxygen vacancy, suggesting a more pronounced enhancement of Fe-O covalency.

3.3. OER performance

We use a three-electrode system to evaluate the electrochemical performance for OER in 1 M KOH electrolyte. The redox kinetics of the catalysts are investigated by cyclic voltammetry (CV) measurements. As shown in Fig. S18, NFO exhibits the highest oxidation potential due to its structurally stable metal that is not easily oxidized, and the other samples show an increasing trend in their oxidation potentials, indicating an increase in the valence state of the metal ions. The F60 exhibits the best OER performance with an overpotential of 271 mV at a current density of 10 mA cm^{-2}, which is lower than that of F30 (303 mV), OV (349 mV), NFO (416 mV) and RuO_2 (322 mV) (Figs. 3a and S19a). The overpotential required for the catalysts to achieve a current density of 1 A cm^{-2} are 341 mV (F60), 428 mV (F30), 637 mV (OV), and 770 mV (NFO), respectively (Fig. S20a). Figs. 3b and S19b show that F60 has the lowest Tafel slope (40.55 mV dec^{-1}), indicating its efficient OER reaction kinetics. The charge transfer resistance in EIS testing primarily reflects the charge transfer kinetics at the electrode/electrolyte interface. The F60 has the smallest charge transfer resistance at 0.5 V, indicating the fastest interfacial charge transfer capability (Fig. 3c). The minimal R_{ct} exhibited of the F60 sample is attributed to its optimized surface, which generates unique active sites.

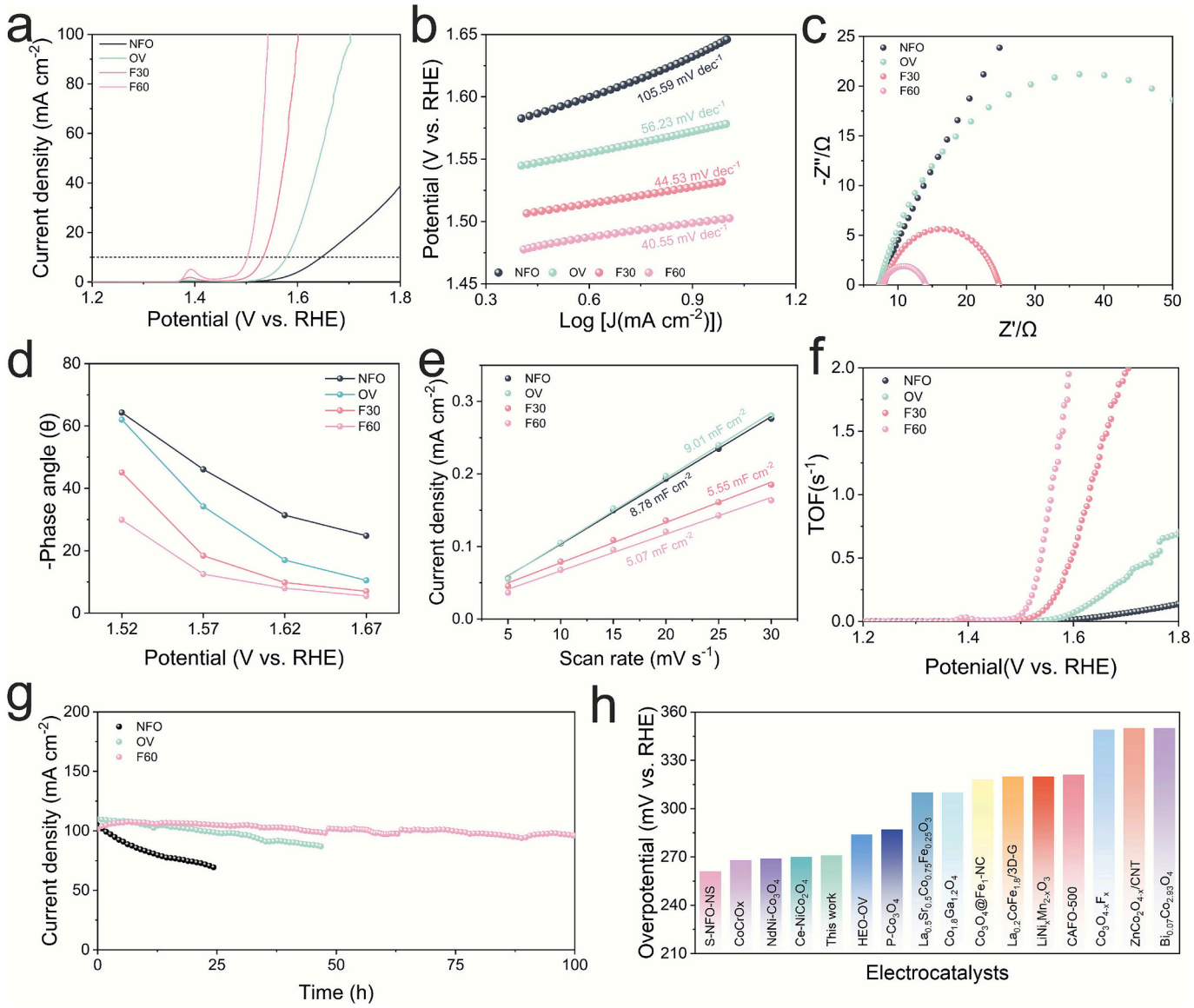

Fig. 3. OER performance of the catalysts. a) LSV curve, b) Tafel slope, c) EIS results of the catalysts. d) The phase angle at different voltages from Bode phase plots. e) The double-layer capacitance, f) Turnover frequency of the catalysts. g) i-t curves of NFO, OV, and F60 at 100 mA cm^{-2}. h) Comparison of OER performance of catalysts.

The electrocatalytic kinetics of the OER process is further examined using EIS tests with different potentials (Figs. 3d and S21). The phase angle of the catalysts is almost unchanged under low potential conditions, suggesting a slower electrochemical oxidation of the catalysts. The phase angle in the low-frequency region corresponds to electrolyte-catalyst interfacial charge transfer in Bode phase plots. An increased potential leads to a decrease in the peak and a simultaneous shift to higher frequencies, representing the charge accumulation and deprotonation process occurring at the surface during the OER process [45,46]. The reduced peak intensities and lower peak intervals of the other samples compared to the pristine NFO indicate an enhanced charge transfer process and accelerated the reaction kinetics. The phase angle in the high-frequency region is related to the intrinsic conductivity of the catalyst. All samples exhibit phase peaks in this region at high bias voltages, indicating that the reaction kinetics are also influenced by the intrinsic conductivity of the catalyst.

The carrier concentrations of the catalysts have been analyzed by Mott-Schottky (Mott-Schottky) curves. It represents bulk electrical conductivity, characterizing the catalyst's ability to transport electrons internally.The slopes of the Mott-Schottky curves of the prepared catalysts are all negative, indicating that the catalysts are all p-type semiconductors (Fig. S22). The carrier concentration of OV is significantly improved compared with that of NFO, which is attributed to the formation of the appropriate amount of oxygen vacancy. These vacancies result from the detachment of metal electrons from covalent bonds to generating free electrons and electron holes that can enhance the conductivity. The concentration of oxygen vacancy in F30 and F60 is excessively high because the oxygen vacancy are in competition with the electron holes. This competition reduces the electron hole content, decreases the carrier concentration, leading to the deterioration of the electrical conductivity [47]. The deterioration in bulk phase conductivity indicates that the performance improvement stems from other factors.

Therefore, the enhancement of F30 and F60 OER performance may be related to its intrinsic activity enhancement. Further by analyzing the double-layer capacitance (C_{dl}) of the catalysts, the C_{dl} values of F30 (5.55 mF cm^{-2}) and F60 (5.07 mF cm^{-2}) are lower than those of NFO (8.78 mF cm^{-2}) and OV (9.01 mF cm^{-2}), indicating that they have the

smallest electrochemical active surface area (ECSA) (Figs. 3e and S23); moreover, F60 exhibits the highest turnover frequency (Fig. 3f), demonstrating an increase in intrinsic activity. This may be related to the specific atomic configurations that modify the intrinsic activity of the catalyst surface.

The stability tests performed on NFO, OV and F60 catalysts demonstrate that F60 exhibits the least performance degradation after 100 h at a current density of 100 mA cm^{-2} (Fig. 3g). And F60 retains 92.6 % of the current density after 70 h of stability test at 500 mA cm^{-2}, which is superior to other catalyst samples (Fig. S20b). Chronopotentiometry measurement of F60 shows negligible overpotential enhancement of the catalyst at 10 mA cm^{-2} and 100 mA cm^{-2} for extended periods (Fig. S24). XRD, TEM, and Raman after OER tests of the catalysts show that the structure is well maintained (Figs. S25–29). The F element content does not significantly change after the stability tests, suggesting that there is no leaching of F-element (Table S6). The XPS results of Ni and Fe for all samples exhibit little change after stability tests, indicating a stable surface chemical state of the catalyst (Fig. S30). The XPS spectra of F also exhibit no significant changes after stability testing, indicating the stable presence of fluorine species throughout the catalytic process (Fig. S31). The F60 catalyst exhibits better performance than most recently reported catalysts (Fig. 3h and Table S7).

3.4. OER mechanism

According to previous reports, tetramethylammonium cation (TMA^+) can interact with active lattice oxygen, so tetramethylammonium cation can serve as a chemical probe to assess the involvement of lattice oxygen in the OER process [48]. It is observed in Fig. 4a that the performance of all catalysts decreases upon the addition of tetramethylammonium hydroxide (TMAOH), and the decrease is attributed to the superoxide radicals on the surface of the lattice oxygen mechanism that are tightly bound to TMA^+, thus limiting the formation of O_2. The NFO exhibits minimal attenuation at low current density but suffers from performance degradation at high current density, attributed to the limited lattice oxygen activity. In contrast, OV, F30 and F60 exhibit a gradual increase in the attenuation after the addition of TMAOH, which proves that the lattice oxygen activity in these catalysts is gradually enhanced. The AEM follows a coupled proton-electron transfer mechanism. In contrast, the LOM typically involves decoupled electron and proton transfers, a process characterized by strongly pH-dependent catalytic activity [9]. We have tested the electrochemical properties of four samples at different pH conditions (pH = 12.5, 13, 13.5, 14) and calculated the proton reaction order (ρ^{RHE}). The ρ^{RHE} of NFO, OV, F30, and F60 are 0.70, 0.82, 0.87, and 0.96, suggesting the presence of LOM for all samples (Figs. 4b and S32). The pH dependence of F60 is the strongest, indicating that it has the strongest lattice oxygen activity. The coupling factor $T^{e^-}_{H^+}$ is obtained to verify the proton (H^+) transfer ability by analyzing the pH and potential (Fig. 4c). F60 has the largest $T^{e^-}_{H^+}$, representing the fastest H^+ transfer kinetics of F60 [49].

Generally, the surface of catalysts with LOM undergo irreversible surface reconfiguration due to the involvement of lattice oxygen atoms in the reaction. Thus, in situ Raman tests (in situ Raman) have been conducted on NFO, OV and F60 to reveal the surface evolution of the catalytic process (Figs. 4d and S33). All the samples exhibit ideal Raman peaks of $NiFe_2O_4$ anti-spinel structure, and the peaks located near 700 cm^{-1}, 570 cm^{-1}, 485 cm^{-1} and 328 cm^{-1} belong to A_{1g}, F_{2g} and E_g vibrational modes arise from the asymmetric bending and stretching of Fe-O bonds. The peak position and intensity of the samples show no significant changes throughout the OER process, and the characteristic peaks of oxyhydroxides are not observed during the test. The results indicate that the catalyst surface does not reconstruct during the catalytic process and the crystal structure remains stable. This is consistent with TEM results after the stability tests (Figs. S25–27).

The adsorption reaction intermediates of the OER process are investigated by in situ attenuated total reflection Fourier transform spectroscopy (in situ ATR FTIR). Two distinct absorption peaks are observed at 1205 cm^{-1} and 1108 cm^{-1}, attributed to the O-O intermediate of LOM and the *OOH intermediate of AEM, respectively (Figs. 4e

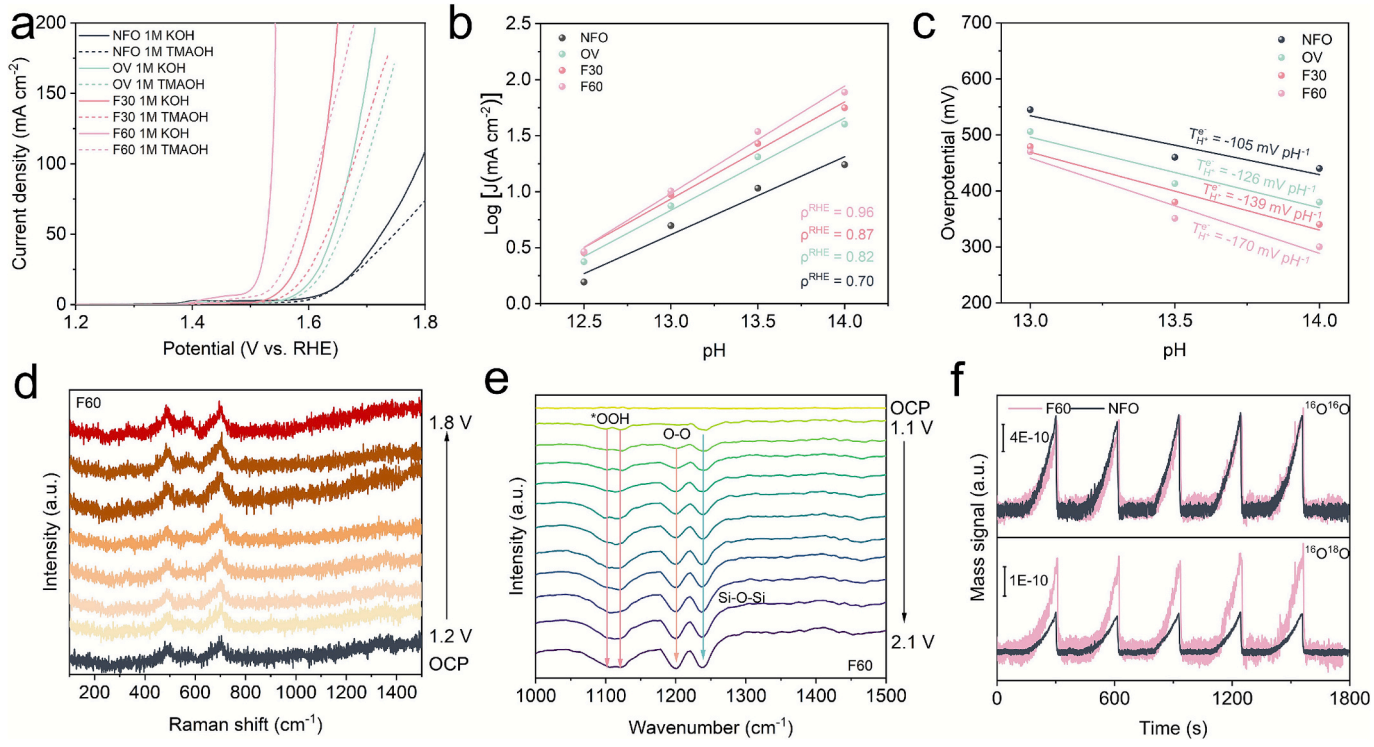

Fig. 4. OER mechanism of the catalysts. a) LSV curves of the catalyst in 1 M KOH and 1 M TMAOH b) pH dependence of the catalyst. c) The coupling factor $T^{e^-}_{H^+}$. d) In situ Raman spectra of F60. e) In situ ATR FTIR spectra of F60. f) DEMS tests of NFO and F60.

and S34) [41]. It is demonstrated that there are two simultaneous mechanisms on the catalyst surface during the OER process [50]. The O-O peak intensity of F60 is significantly increased compared with NFO and OV, indicating enhanced LOM activity. The peak of *OOH has a distinct companion peak at around 1126 cm^{-1}, originating from the effect of the hydrogen bonds of *OOH with the neighbor metal sites. The hydrogen bond peak of *OOH in F60 is more pronounced, and the presence of hydrogen bonds is more conducive to the deprotonation process of the *OOH intermediate, thereby accelerating the AEM. The result suggests the ability to promote both AEM and LOM under the influence of vacancy and F doping.

DEMS tests further demonstrates the coupling of AEM and LOM mechanisms. $^{16}O^{16}O$ and $^{16}O^{18}O$ correspond to the O_2 products of the AEM and LOM (involving one lattice oxygen) pathways, respectively. Both NFO and F60 detected distinct $^{16}O^{16}O$ and $^{16}O^{18}O$ signals, confirming the cooperative action of AEM and LOM (Fig. 4f). The signal intensity of $^{16}O^{18}O$ in F60 is higher than that in NFO, demonstrating higher activity of its lattice oxygen. Meanwhile, the signal intensity of $^{16}O^{16}O$ shows no significant difference between the two samples, indicating that while the proportion of the LOM mechanism increases, the activity of the AEM mechanism has not decreased. This suggests that the catalyst's catalytic mechanism involves a coupling of AEM and LOM.

3.5. Theoretical calculation analysis

The effects of vacancy modification and fluorine doping on the catalytic activity of the (2 2 0) and (3 1 1) crystal plane of $NiFe_2O_4$ are elucidated by theoretical calculations. Based on the EPR test results, we chose one oxygen vacancy to modify the (2 2 0) plane (named OV) and two oxygen vacancies co-modified with an F atom to modify the (2 2 0) plane (named F-OV-220) and the (3 1 1) plane (named F-OV-311). Based on the results of EXAFS analysis, we select the positions located at the centers of Ni-O octahedron and Fe-O octahedron and Fe-O tetrahedron as the doping positions of F atom.

Calculations of the systematic bader charge reveal that the charge density of the F-OV-311 metal atoms is the lowest, suggesting that the average valence state of F-OV-311 is the highest (Figs. S35 and S36). The bader charge analysis provides evidence for the redistribution of the surface charge induced by the fluorine anion and oxygen vacancy. Fig. S36a,b indicate that the valence states of some surface metal atoms

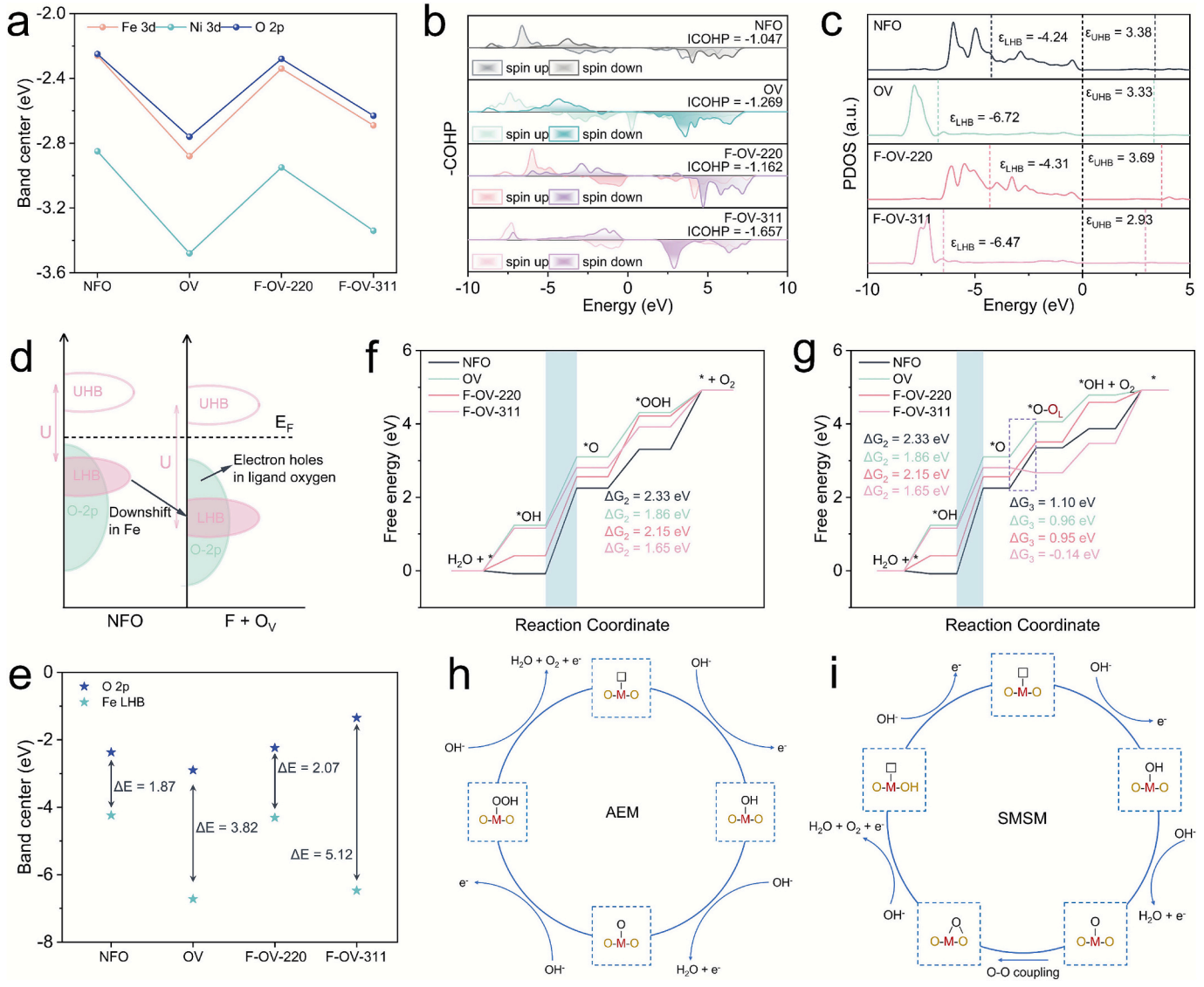

Fig. 5. Analysis of DFT calculations. a) Distribution of energy band center. b) COHP of Fe-O bond. c) Distribution of LHB and UHB of Fe sites. d) Schematic of the energy band structure. e) Distribution of O 2*p* and Fe LHB. Gibbs free energy diagram for the f) AEM mechanism and g) SMSM mechanism. Schematic of the reaction paths for the h) AEM mechanism and i) SMSM mechanism.

also increase compared to the original NFO in the presence of oxygen vacancies. However, the overall bader charge values for the OV are higher than those for the NFO, indicating a larger overall electron density (Fig. S35). This aligns with XPS and XANES results.

The projected density of states (PDOS) reveals that the band center of Fe 3*d* orbital of NFO, OV, F-OV-220, and F-OV-311 are close to that of the O 2*p* orbital. This significant overlap indicates strong covalency in the Fe-O bond (Figs. 5a and S37) [51]. In contrast, the *3d* band center of Ni is positioned further from the Fermi energy level and the O 2*p* orbital compared to Fe, resulting in a lower degree of covalency for the Ni-O bond. Further calculations of Crystal orbital Hamilton populations (COHP) for Fe-O and Ni-O bond show that the ICOHP for Ni-O is larger than that for Fe-O, proving that the covalency of Fe-O bond is stronger than the Ni-O bond (Figs. 5b and S38a). Statistical analysis of ICOHP at all metal sites on the surface indicates that the average ICOHP (−1.455) of Fe-O in the F-OV-311 model also exhibits the most negative value (compared to NFO -1.107, OV -1.269, and F-OV-220 -1.149 in other models) (Tables S8-S11). It demonstrates that the synergistic effect of fluorine anion and oxygen vacancy on the (3 1 1) plane significantly enhances Fe-O covalency. The Fe-O bond of F-OV-311 has the smallest ICOHP value, indicating that it has the strongest covalency, which is conducive to the promotion of electron delocalization, accelerating the deprotonation process, and enhancing catalytic activity [52,53]. The catalyst ICOHP exhibits a coupled variation trend with overpotential, indicating an intrinsic relationship between the covalent nature of Fe-O bonds and catalytic activity (Fig. S39).

The molecular orbitals for Metal-Oxygen can be divided into bonding orbitals (M-O) and antibonding orbitals (M-O)*. The (M-O)* splits into electron-filled low Hubbard energy bands (LHB) and empty high Hubbard energy bands (UHB) due to the strong *d-d* Coulomb interaction (U) [10]. The U of NFO, OV, F-OV-220, and F-OV-311 are 7.62 eV, 9.05 eV, 8.00 eV, and 9.40 eV, respectively (Fig. 5c). The modification of oxygen vacancy and F atom increases U which affects the relative positions of the LHB and UHB. The PDOS of O 2*p* is shown in Fig. S38b, the LHB is positioned far away from the Fermi energy level and the center of the O 2*p* orbital. The energy difference between the LHB and the O 2*p* orbital gradually increases, facilitating the formation of ligand holes as the oxygen ligands lose electrons. The Fe LHB and O 2*p* band center offset in the F-OV-311 model is 5.12 eV, that is higher than other models (NFO: 1.87 eV, OV: 3.82 eV, F-OV-220: 2.07 eV). This process promotes electron transfer between the metal and the ligand oxygen (Fig. 5d,e) [37]. The ligand holes enhance the electrophilicity and redox activity of the oxygen ligand and enhance the ability of oxygen to participate in the reaction. As the deviation of its band center increases, ICOHP becomes more negative. Therefore, the deviation of the LHB and O 2*p* band centers may serve as parameters for measuring covalency (Fig. S40). Meanwhile, the surface oxygen vacancy formation energy of F-OV-311 is lower, which facilitates the LOM pathway (Fig. S41).

In order to elucidate the role of oxygen vacancy and fluorine anion at the (3 1 1) crystal plane, we additionally calculate the electronic structure of NFO-311, OV-311 and F-311. The analysis results indicate that the U of NFO-311, OV-311, F-311 and F-OV-311 are 9.26 eV, 9.24 eV, 9.72 eV and 9.40 eV, and the O 2*p* band centers are −1.64 eV, −1.34 eV, −1.60 eV and − 1.35 eV, respectively (Fig. S42a,b). This demonstrates that the oxygen vacancy has a minimal effect on the *d-d* Coulomb interaction, significantly influences the shift of the O 2*p* orbital toward the Fermi energy level, increasing its redox activity. F doping produces minimal changes in the position of the O 2*p* orbital but increases the *d-d* Coulomb interaction, the LHB away from the Fermi energy level, enlarges the gap between O 2*p* and the LHB, and enhances M-O covalency (Fig. S42c).

The adsorption energy of *OH at metal site and oxygen site of different models is analyzed (Fig. S43). The results reveal that the adsorption energy of all models at the metal site are lower than those at the oxygen site, indicating that *OH is more suitable for adsorption at the metal site. This preference prevents the occurrence of OVSM by avoiding the direct adsorption of intermediates at the oxygen site. Therefore, we propose that the catalysts should follow AEM and SMSM with adsorbing *OH at metal site serving as the active center and the starting point of the catalytic pathway. We calculate the OER Gibbs free energy diagrams of AEM and SMSM paths (Fig. 5f,g). Fig. 5h,i illustrates the reaction mechanism pathways for AEM and SMSM. The results indicate that the rate-determining step (RDS) of both mechanisms is the deprotonation process of *OH. F-OV-311 has the lowest energy barrier for the deprotonation process (ΔG = 1.65 eV). With the change of M-O bond covalency, the energy barrier for O-O coupling in the LOM mechanism of the corresponding catalyst decreases. Notably, F-OV-311 exhibits the lowest change in O-O coupling Gibbs free energy (ΔG = −0.14 eV). This demonstrates the positive effect of increased M-O covalency in enhancing the reactivity of AEM and SMSM.

Adsorption models show that the intermediates adsorb on the (2 2 0) plane at adjacent octahedrally coordinated Ni and Fe, whereas on the (3 1 1) plane they preferentially adsorb on adjacent tetrahedrally and octahedrally coordinated Fe sites connected by F atom (Fig. S44). To demonstrate that Fe_{Oh}-F-Fe_{Td} is the best adsorption site, we also calculate the deprotonation energy barrier on Fe_{Oh}-O-Fe_{Td}, Ni_{Oh}-O-Fe_{Td}, Ni_{Oh}-F-Fe_{Td}, Fe_{Oh}-F-Ni_{Oh} and Fe_{Oh}-O-Ni_{Oh} (Figs. S45 and S46). The energy barrier for the deprotonation process on these configurations is higher (ΔG = 2.08 eV, 2.13 eV, 1.99 eV, 2.15 eV and 2.41 eV), so the special configuration of Fe_{Oh}-F-Fe_{Td} plays an important role in optimizing the adsorption of the reaction intermediates and lowering the energy barrier. The results suggest that the decrease in electrochemically active area and the increase in intrinsic activity may be attributed to this particular configuration. The analysis of the ICOHP of the M-O bonds on the surface of both configurations also indicates that the covalency of the Fe-O bond of the F-atom-bridged configuration is higher than that in the O-atom-bridged configuration (Fig. S47). This enhanced covalency facilitates electron transfer between the catalyst and the intermediates, thereby lowering the energy barrier in the OER process [54].

3.6. Performance of AEMWE devices

To evaluate the electrocatalytic performance of the prepared F60 catalyst under simulated industrial conditions, an anion-exchange membrane electrolyzer (AEMWE) was constructed using commercial Pt/C and F60 catalysts as the cathode and anode, respectively. For comparison, AEMWE using a commercial RuO_2 as anode was constructed. Fig. 6a shows a schematic diagram of AEMWE. The polarization curves in Fig. 6b demonstrate that the Pt/C||F60 electrolyzer exhibits significantly superior catalytic performance compared to Pt/C||RuO_2. The voltages required for F60 to achieve current densities of 1 A cm^{-2} and 2 A cm^{-2} are 2.09 V and 2.35 V, respectively, which are substantially lower than the 2.37 V and 2.80 V of commercial RuO_2. This further confirms the exceptional catalytic activity of the constructed dual-mechanism catalyst. The AEMWE constructed with F60 as the anode operated for 300 h at a current density of 1 A cm^{-2}, exhibiting minimal potential shift, which confirms the catalyst's outstanding structural stability (Fig. 6c). In conclusion, owing to the coupling of the dual catalytic mechanisms of AEM and SMSM, the designed F60 catalyst exhibits high activity and stability in AEMWE.

4. Conclusion

In summary, we designed $NiFe_2O_4$ catalysts with the incorporation of fluorine anion and oxygen vacancy through NH_4F-assisted pyrolysis. The activity of AEM and SMSM is improved by introducing Fe-F-Fe configuration and oxygen vacancy. Experimental and theoretical calculations demonstrate that the Fe-O covalency is enhanced with the optimization of energy positions of the LHB and O 2*p* band center by the modulation of fluorine anion and oxygen vacancy. The deprotonation ability of the Fe-F-Fe site and the activity of the lattice oxygen are enhanced, with the O-O coupling energy barrier is significantly reduced.

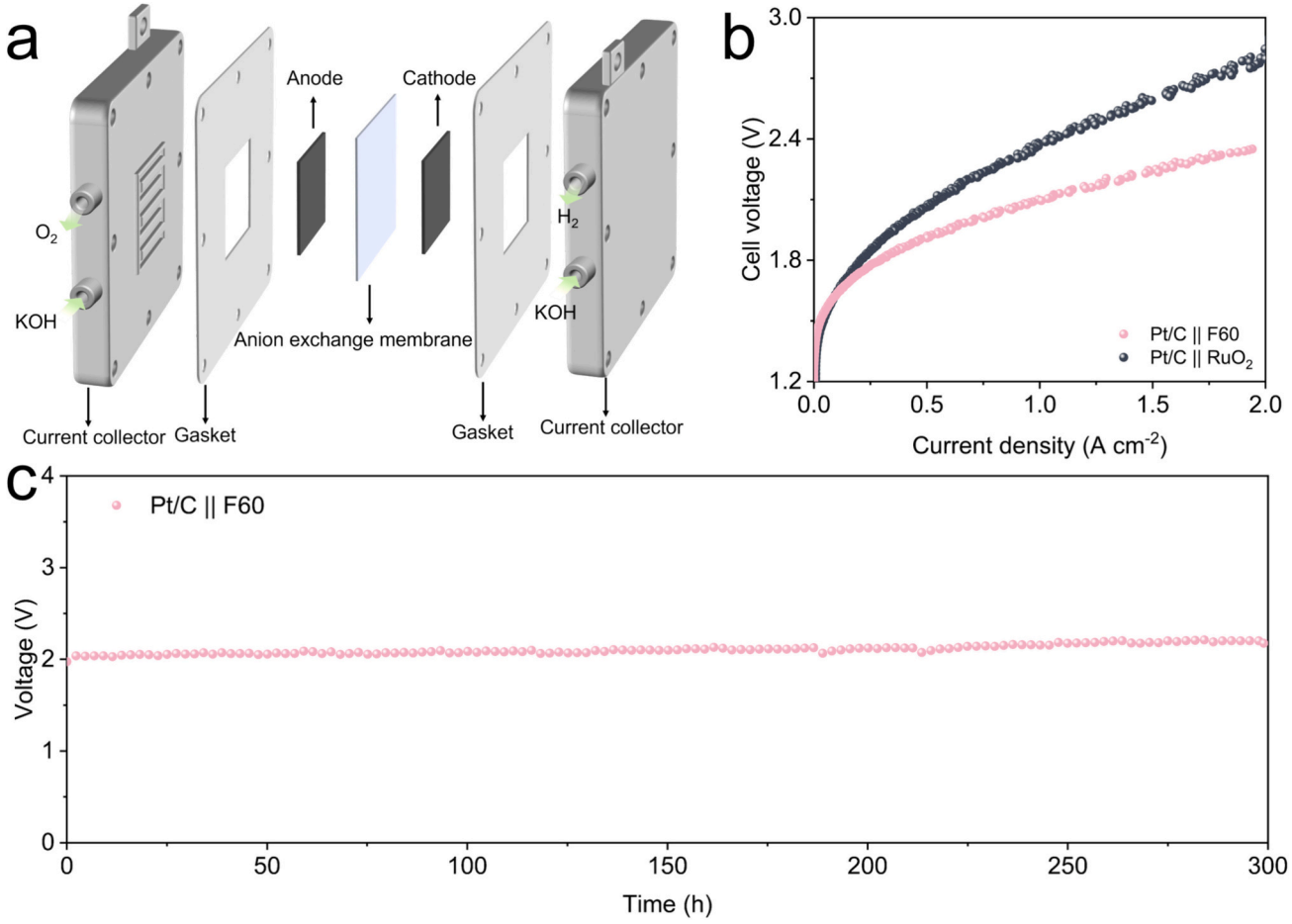

Fig. 6. Performance of AEMWE devices. a) Schematic diagram of AEMWE. b) Polarization curves of AEMWE. c) Chronopotentiometry test.

The Fe_{Oh}-F-Fe_{Td} on the (3 1 1) crystal plane exhibits moderate adsorption of reaction intermediates and the lowest deprotonation energy barrier, resulting in optimal reactivity. Therefore, the F60 catalyst has an excellent catalytic performance (271 mV@10 mA cm^{-2}). This work develops a high-performance OER catalyst for alkaline environment and identifies the active sites and mechanisms on the catalyst surface for enhanced catalysis, which is instructive for the synthesis of efficient catalysts.

CRediT authorship contribution statement

Bo Feng: Writing – original draft, Validation, Methodology, Data curation. **Keyi Lv:** Investigation. **Ziyong Zhang:** Investigation. **Nianwen Song:** Investigation. **Ziyang Yan:** Investigation. **Yuchao Zhang:** Investigation. **Yanfei Wei:** Investigation. **Xiaofei Yu:** Investigation. **Lanlan Li:** Investigation. **Xinghua Zhang:** Investigation. **Xiaojing Yang:** Investigation. **Zunming Lu:** Writing – review & editing, Supervision, Methodology, Funding acquisition. **Juntao Huo:** Supervision.

Declaration of competing interest

The authors declare that they have no known competing financial interests or personal relationships that could have appeared to influence the work reported in this paper.

Data availability

Data will be made available on request.

Acknowledgment

This work was supported by the National Natural Science Foundation of China (No. 52171176, No. U24A2039, No. 52571244, No. 52271210, No. 22179032), the Natural Science Foundation of Tianjin Municipality (No. 23JCZDJC00420), and the Hebei Provincial Department of Science and Technology (No. 246Z4415G).

Appendix A. Supplementary data

Supplementary data to this article can be found online at https://doi.org/10.1016/j.cej.2025.171300.

References

[1] H. Li, Y. Lin, J. Duan, Q. Wen, Y. Liu, T. Zhai, Stability of electrocatalytic OER: from principle to application, Chem. Soc. Rev. 53 (2024) 10709–10740, https://doi.org/10.1039/d3cs00010a.
[2] Y. Jiang, S. Gao, X. Liu, Y. Wang, S. Zhou, Q. Liu, A. Abdukayum, G. Hu, Recent achievements in selenium-based transition metal electrocatalysts for pH-universal water splitting, Nano Res. 17 (2024) 5763–5785, https://doi.org/10.1007/s12274-024-6485-9.
[3] J.O. Olowoyo, R.J. Kriek, Recent progress on bimetallic-based spinels as electrocatalysts for the oxygen evolution reaction, Small 18 (2022) 2203125, https://doi.org/10.1002/smll.202203125.
[4] Y. Zhang, Q. Fu, B. Song, P. Xu, Regulation strategy of transition metal oxide-based electrocatalysts for enhanced oxygen evolution reaction, Acc. Mater. Res. 3 (2022) 1088–1100, https://doi.org/10.1021/accountsmr.2c00161.
[5] Q. Ji, B. Tang, X. Zhang, C. Wang, H. Tan, J. Zhao, R. Liu, M. Sun, H. Liu, C. Jiang, J. Zeng, X. Cai, W. Yan, Operando identification of the oxide path mechanism with different dual-active sites for acidic water oxidation, Nat. Commun. 15 (2024) 8089, https://doi.org/10.1038/s41467-024-52471-7.
[6] Z.-F. Huang, J. Song, Y. Du, S. Xi, S. Dou, J.M.V. Nsanzimana, C. Wang, Z.J. Xu, X. Wang, Chemical and structural origin of lattice oxygen oxidation in Co–Zn

oxyhydroxide oxygen evolution electrocatalysts, Nat. Energy 4 (2019) 329–338, https://doi.org/10.1038/s41560-019-0355-9.
[7] C. Lin, J.-L. Li, X. Li, S. Yang, W. Luo, Y. Zhang, S.-H. Kim, D.-H. Kim, S.S. Shinde, Y.-F. Li, Z.-P. Liu, Z. Jiang, J.-H. Lee, In-situ reconstructed Ru atom array on α-MnO_2 with enhanced performance for acidic water oxidation, Nat. Catal. 4 (2021) 1012–1023, https://doi.org/10.1038/s41929-021-00703-0.
[8] Z.H. Yin, Y. Huang, K. Song, T.T. Li, J.Y. Cui, C. Meng, H. Zhang, J.J. Wang, Ir single atoms boost metal-oxygen covalency on selenide-derived NiOOH for direct intramolecular oxygen coupling, J. Am. Chem. Soc. 146 (2024) 6846–6855, https://doi.org/10.1021/jacs.3c13746.
[9] X. Wang, H. Zhong, S. Xi, W.S.V. Lee, J. Xue, Understanding of oxygen redox in the oxygen evolution reaction, Adv. Mater. 34 (2022) e2107956, https://doi.org/10.1002/adma.202107956.
[10] Y. Zhang, W. Zhang, X. Zhang, X. Wang, J. Wang, Q. Zhao, Y. Sun, J. Li, G. Liu, X. Han, Activating lattice oxygen based on energy band engineering in oxides for industrial water/saline oxidation, Energ. Environ. Sci. 17 (2024) 3347–3357, https://doi.org/10.1039/d4ee00214h.
[11] J. Chang, Y. Shi, H. Wu, J. Yu, W. Jing, S. Wang, G.I.N. Waterhouse, Z. Tang, S. Lu, Oxygen radical coupling on short-range ordered Ru atom arrays enables exceptional activity and stability for acidic water oxidation, J. Am. Chem. Soc. 146 (2024) 12958–12968, https://doi.org/10.1021/jacs.3c13248.
[12] W. Zhang, H. Cao, X. Wen, L. Ma, Z. Zhang, Z. Xu, X. Luo, Dual-site bridging mechanism for bimetallic electrochemical oxygen evolution, Angew. Chem. Int. Ed. Engl. 136 (2024) e202411683, https://doi.org/10.1002/anie.202411683.
[13] B. Yao, Y. Chen, Y. Yan, Y. Yang, H. Xing, Y. Xu, D. Jiao, Z. Xing, D. Wang, X. Yang, Iron-induced localized oxide path mechanism enables efficient and stable water oxidation, Angew. Chem. Int. Ed. Engl. 64 (2024) e202416141, https://doi.org/10.1002/anie.202416141.
[14] J. Yang, K. An, Z. Yu, L. Qiao, Y. Cao, Y. Zhuang, C. Liu, L. Li, L. Peng, H. Pan, Effect of cation and anion vacancies in ruthenium oxide on the activity and stability of acidic oxygen evolution, ACS Catal. 14 (2024) 17739–17747, https://doi.org/10.1021/acscatal.4c02779.
[15] W. Hu, B. Huang, M. Sun, J. Du, Y. Hai, W. Yin, X. Wang, W. Gao, C. Zhao, Y. Yue, Z. Li, C. Li, Doping Ti into RuO_2 to accelerate bridged-oxygen-assisted deprotonation for acidic oxygen evolution reaction, Adv. Mater. 37 (2024) e2411709, https://doi.org/10.1002/adma.202411709.
[16] J. Choi, D. Kim, S.J. Hong, X. Zhang, H. Hong, H. Chun, B. Han, L.Y.S. Lee, Y. Piao, Tuning the electronic structure and inverse degree of inverse spinel ferrites by integrating samarium orthoferrite for efficient water oxidation, Appl. Catal. Environ. 315 (2022) 121504, https://doi.org/10.1016/j.apcatb.2022.121504.
[17] Y. Peng, C. Huang, J. Huang, M. Feng, X. Qiu, X. Yue, S. Huang, Filling octahedral interstices by building geometrical defects to construct active sites for boosting the oxygen evolution reaction on $NiFe_2O_4$, Adv. Funct. Mater. 32 (2022) 2201011, https://doi.org/10.1002/adfm.202201011.
[18] Y. Li, Z. Zhang, C. Li, X. Hou, J. Zeng, X.B. Chen, Z. Shi, S. Feng, Cation-vacancy-induced reinforced electrochemical surface reconstruction on spinel nickel ferrite for boosting water oxidation, Adv. Funct. Mater. 35 (2024) 2417983, https://doi.org/10.1002/adfm.202417983.
[19] D. Li, D. Xu, Y. Pei, Q. Zhang, Y. Lu, B. Zhang, Isolated octahedral Pt-induced electron transfer to ultralow-content ruthenium-doped spinel Co_3O_4 for enhanced acidic overall water splitting, J. Am. Chem. Soc. 146 (2024) 28728–28738, https://doi.org/10.1021/jacs.4c07089.
[20] Y. Liu, C. Ye, L. Chen, J. Fan, C. Liu, L. Xue, J. Sun, W. Zhang, X. Wang, P. Xiong, J. Zhu, High entropy-driven role of oxygen vacancies for water oxidation, Adv. Funct. Mater. 34 (2024) 2314820, https://doi.org/10.1002/adfm.202314820.
[21] A.A. Yadav, Y.M. Hunge, S.B. Kulkarni, C. Terashima, S.-W. Kang, Three-dimensional nanoflower–like hierarchical array of multifunctional copper cobaltate electrode as efficient electrocatalyst for oxygen evolution reaction and energy storage application, J. Colloid Interface Sci. 576 (2020) 476–485, https://doi.org/10.1016/j.jcis.2020.04.100.
[22] L. Sun, M. Feng, Y. Peng, X. Zhao, Y. Shao, X. Yue, S. Huang, Constructing oxygen vacancies by doping Mo into spinel Co_3O_4 to trigger a fast oxide path mechanism for acidic oxygen evolution reaction, J. Mater. Chem. A 12 (2024) 8796–8804, https://doi.org/10.1039/d4ta00655k.
[23] D. Chen, R. Yu, H. Zhao, J. Jiao, X. Mu, J. Yu, S. Mu, Boron-induced interstitial effects drive water oxidation on ordered Ir-B compounds, Angew. Chem. Int. Ed. Engl. 63 (2024) e202407577, https://doi.org/10.1002/anie.202407577.
[24] N. Zhao, W. Luo, S. Li, H. Wang, Y. Mao, Y. Jiang, W. Wang, M. Li, W. Su, R. He, Strong bonding of lattice N activates metal Ni to achieve efficient water splitting, Adv. Sci. 12 (2024) e2411526, https://doi.org/10.1002/advs.202411526.
[25] X. Tao, L. Hou, X. Wang, J. Jin, H. Li, F. Gao, Iron and oxygen vacancies co-modulated adsorption evolution and lattice oxygen dual-path mechanism for water oxidation, Nat. Commun. 16 (2025) 8788, https://doi.org/10.1038/s41467-025-63844-x.
[26] J. Nie, J. Shi, L. Li, M.Y. Xie, Z.Y. Ouyang, M.H. Xian, G.F. Huang, H. Wan, W. Hu, W.Q. Huang, Anion-mediated rapid and direct synthesis of FeNiOOH for robust water oxidation, Adv. Funct. Mater. 35 (2024) 2414493, https://doi.org/10.1002/adfm.202414493.
[27] J.P. Perdew, K. Burke, M.J.P.r.l. Ernzerhof, Generalized gradient approximation made simple, Phys. Rev. Lett. 77 (1996) 3865, https://doi.org/10.1103/PhysRevLett.77.3865.
[28] J.P. Perdew, K. Burke, Y.J.P.r.B. Wang, Generalized gradient approximation for the exchange-correlation hole of a many-electron system, Phys. Rev. B 54 (1996) 16533, https://doi.org/10.1103/PhysRevB.54.16533.
[29] Y. Duan, S. Sun, Y. Sun, S. Xi, X. Chi, Q. Zhang, X. Ren, J. Wang, S.J.H. Ong, Y. Du, L. Gu, A. Grimaud, Z.J. Xu, Mastering surface reconstruction of metastable spinel oxides for better water oxidation, Adv. Mater. 31 (2019) 1807898, https://doi.org/10.1002/adma.201807898.
[30] Y. Yan, J. Lin, K. Huang, X. Zheng, L. Qiao, S. Liu, J. Cao, S.C. Jun, Y. Yamauchi, J. Qi, Tensile strain-mediated spinel ferrites enable superior oxygen evolution activity, J. Am. Chem. Soc. 145 (2023) 24218–24229, https://doi.org/10.1021/jacs.3c08598.
[31] S. Zhu, X. Wang, J. Le, N. An, J. Li, D. Liu, Y. Kuang, Striking stabilization effect of spinel cobalt oxide oxygen evolution electrocatalysts in neutral pH by dual-sites Iron incorporation, Energy Environ. Mater. 7 (2023) e12594, https://doi.org/10.1002/eem2.12594.
[32] R. Dronskowski, P. Bloechl, Crystal orbital Hamilton populations (COHP): energy-resolved visualization of chemical bonding in solids based on density-functional calculations, J. Phys. Chem. 97 (1993) 8617–8624, https://doi.org/10.1021/j100135a014.
[33] Y. Wang, P. Guo, J. Zhou, B. Bai, Y. Li, M. Li, P. Das, X. Wu, L. Zhang, Y. Cui, J. Xiao, Z.-S. Wu, Tuning the Co pre-oxidation process of Co_3O_4 via geometrically reconstructed F–Co–O active sites for boosting acidic water oxidation, Energ. Environ. Sci. 17 (2024) 8820–8828, https://doi.org/10.1039/d4ee03982c.
[34] K. Xiao, Y. Wang, P. Wu, L. Hou, Z.Q. Liu, Activating lattice oxygen in spinel $ZnCo_2O_4$ through filling oxygen vacancies with fluorine for electrocatalytic oxygen evolution, Angew. Chem. Int. Ed. 62 (2023) e202301408, https://doi.org/10.1002/anie.202301408.
[35] Y. Li, H. Guo, J. Zhao, Y. Zhang, L. Zhao, R. Song, Te-doped $NiFe_2O_4$ stabilized by amorphous carbon layers derived from one-step topological transitions of NiFe LDHs with significantly enhanced oxygen evolution reaction, Chem. Eng. J. 464 (2023) 142604, https://doi.org/10.1016/j.cej.2023.142604.
[36] X. Wang, J. Luo, Y. Tuo, Y. Gu, W. Liu, S. Wang, Y. Zhou, J. Zhang, Hierarchical heterostructure of $NiFe_2O_4$ nanoflakes grown on the tip of $NiCo_2O_4$ nanoneedles with enhanced interfacial polarization effect to achieve highly efficient electrocatalytic oxygen evolution, Chem. Eng. J. 457 (2023) 141169, https://doi.org/10.1016/j.cej.2022.141169.
[37] N. Zhang, X. Feng, D. Rao, X. Deng, L. Cai, B. Qiu, R. Long, Y. Xiong, Y. Lu, Y. Chai, Lattice oxygen activation enabled by high-valence metal sites for enhanced water oxidation, Nat. Commun. 11 (2020) 4066, https://doi.org/10.1038/s41467-020-17934-7.
[38] L. Li, X. Zhang, M. Humayun, X. Xu, Z. Shang, Z. Li, M.F. Yuen, C. Hong, Z. Chen, J. Zeng, M. Bououdina, K. Temst, X. Wang, C. Wang, Manipulation of electron spins with oxygen vacancy on amorphous/crystalline composite-type catalyst, ACS Nano 18 (2023) 1214–1225, https://doi.org/10.1021/acsnano.3c12133.
[39] C. Ye, H. Cheng, L. Zheng, J. Lin, Q. Xu, Y. Qiu, Z. Pan, Y. Qiu, Tailoring metal-oxygen bonds boosts oxygen reaction kinetics for high-performance zinc-air batteries, Nano Lett. 23 (2023) 1573–1581, https://doi.org/10.1021/acs.nanolett.3c00053.
[40] H.-B. Zheng, S.-Q. Jing, Y.-L. Wang, P.-Z. Gao, H. Qin, D.-Y. Li, W.-M. Guo, X.-P. Liu, H.-N. Xiao, Oxygen vacancy for boosted alkaline oxygen evolution under AC magnetic field, Int. J. Hydrogen Energy 51 (2023) 511–523, https://doi.org/10.1016/j.ijhydene.2023.08.244.
[41] N. Yao, N. Luo, S. Jiang, A. Cai, W. Pi, X. Wang, Manipulated reaction route for oxyhydroxides toward top-performing water oxidation via eg electron filling state, Adv. Funct. Mater. 34 (2024) 2405474, https://doi.org/10.1002/adfm.202405474.
[42] H. Wang, T. Zhai, Y. Wu, T. Zhou, B. Zhou, C. Shang, Z. Guo, High-valence oxides for high performance oxygen evolution electrocatalysis, Adv. Sci. 10 (2023) e2301706, https://doi.org/10.1002/advs.202301706.
[43] T. Zhang, Y. Liu, L. Tong, J. Yu, S. Lin, Y. Li, H.J. Fan, Oxidation state engineering in octahedral Ni by anchored sulfate to boost intrinsic oxygen evolution activity, ACS Nano 17 (2023) 6770–6780, https://doi.org/10.1021/acsnano.2c12810.
[44] R. Chen, Z. Wang, S. Chen, W. Wu, Y. Zhu, J. Zhong, N. Cheng, Activating lattice oxygen in spinel oxides via engineering octahedral sites for oxygen evolution, ACS Energy Lett. 8 (2023) 3504–3511, https://doi.org/10.1021/acsenergylett.3c01030.
[45] Z. Liang, D. Shen, Y. Wei, F. Sun, Y. Xie, L. Wang, H. Fu, Modulating the electronic structure of cobalt-vanadium bimetal catalysts for high-stable anion exchange membrane water electrolyzer, Adv. Mater. 36 (2024) 2408634, https://doi.org/10.1002/adma.202408634.
[46] Y. Hao, S.-F. Hung, W.-J. Zeng, Y. Wang, C. Zhang, C.-H. Kuo, L. Wang, S. Zhao, Y. Zhang, H.-Y. Chen, S. Peng, Switching the oxygen evolution mechanism on atomically dispersed Ru for enhanced acidic reaction kinetics, J. Am. Chem. Soc. 145 (2023) 23659–23669, https://doi.org/10.1021/jacs.3c07777.
[47] Q. Ji, L. Bi, J. Zhang, H. Cao, X.S. Zhao, The role of oxygen vacancies of ABO_3 perovskite oxides in the oxygen reduction reaction, Energ. Environ. Sci. 13 (2020) 1408–1428, https://doi.org/10.1039/d0ee00092b.
[48] P. Wang, C. Zhang, J. Ding, Y. Ji, Y. Li, W. Zhang, Motivating inert strontium manganate with iridium dopants as efficient electrocatalysts for oxygen evolution in acidic electrolyte, Small 20 (2023) 2305662, https://doi.org/10.1002/smll.202305662.
[49] X. Wang, J. Hu, T. Lu, H. Wang, D. Sun, Y. Tang, H. Li, G. Fu, Importing atomic rare-earth sites to activate lattice oxygen of spinel oxides for electrocatalytic oxygen evolution, Angew. Chem. Int. Ed. Engl. 64 (2024) e202415306, https://doi.org/10.1002/anie.202415306.
[50] X. Luo, H. Zhao, X. Tan, S. Lin, K. Yu, X. Mu, Z. Tao, P. Ji, S. Mu, Fe-S dually modulated adsorbate evolution and lattice oxygen compatible mechanism for water oxidation, Nat. Commun. 15 (2024) 8293, https://doi.org/10.1038/s41467-024-52682-y.
[51] B. Ge, P. Jiang, B. Chen, C. Huang, Controlling co 3d/O 2p orbital hybridization in $LaCoO_3$ by modulating the co–O–co bond angle for enhanced oxygen evolution

reaction catalysis, ACS Catal. 15 (2024) 477–486, https://doi.org/10.1021/acscatal.4c05479.

[52] P. Zhai, C. Wang, Y. Zhao, Y. Zhang, J. Gao, L. Sun, J. Hou, Regulating electronic states of nitride/hydroxide to accelerate kinetics for oxygen evolution at large current density, Nat. Commun. 14 (2023) 1873, https://doi.org/10.1038/s41467-023-37091-x.

[53] H. Su, C. Yang, M. Liu, X. Zhang, W. Zhou, Y. Zhang, K. Zheng, S. Lian, Q. Liu, Tensile straining of iridium sites in manganese oxides for proton-exchange membrane water electrolysers, Nat. Commun. 15 (2024) 95, https://doi.org/10.1038/s41467-023-44483-6.

[54] Z. Li, X. Li, M. Wang, Q. Wang, P. Wei, S. Jana, Z. Liao, J. Yu, F. Lu, T. Liu, G. Wang, KIr_4O_8 nanowires with rich hydroxyl promote oxygen evolution reaction in proton exchange membrane water electrolyzer, Adv. Mater. 36 (2024) e2402643, https://doi.org/10.1002/adma.202402643.